Tunable Optical Excitations in Twisted Bilayer Graphene Form Strongly Bound Excitons

Hiral Patel,[†] Robin W. Havener,[‡,§] Lola Brown,[‡,§] Yufeng Liang,[∥] Li Yang,[∥] Jiwoong Park,[‡,§] and Matt W. Graham*,[†]

[†]Department of Physics, Oregon State University, Corvallis, Oregon 97331, United States
[‡]Department of Chemistry & Chemical Biology, Cornell University, Ithaca, New York 14850, United States
[§]Kavli Institute at Cornell for Nanoscale Science, Ithaca, New York 14853, United States
[∥]Department of Physics, Washington University in St. Louis, St. Louis, Missouri 63130, United States

S *Supporting Information*

ABSTRACT: When two sheets of graphene stack in a twisted bilayer graphene (tBLG) configuration, the resulting constrained overlap between interplanar 2p orbitals produce angle-tunable electronic absorption resonances. By applying a novel combination of multiphoton transient absorption (TA) microscopy and TEM, we resolve the electronic structure and ensuing relaxation by probing resonant excitations of single tBLG domains. Strikingly, we find that the transient electronic population in resonantly excited tBLG domains is enhanced many fold, forming a major electronic relaxation bottleneck. Two-photon TA microscopy shows this bottleneck effect originates from a strongly bound, dark exciton state lying ~0.37 eV below the 1-photon absorption resonance. This stable coexistence of strongly bound excitons alongside free-electron continuum states has not been previously observed in a metallic, 2D material.

KEYWORDS: Graphene, ultrafast microscopy, ghost Fano resonance, excitons
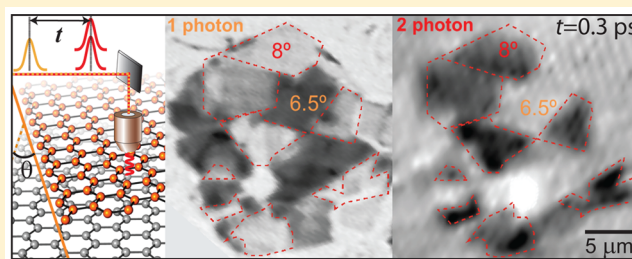
Photoexcited electrons in graphene relax energetically far faster than the $e-h$ separation time scale, making many electronic and optoelectronic applications prohibitive.[1−4] While similar fast, picosecond relaxation time scales are also observed in Bernal stacked bilayer graphene (bBLG),[5] slower relaxation might be possible in twisted bilayer graphene (tBLG). In tBLG, an off-axis interlayer twist angle (θ) gives rise to band anticrossings and van Hove singularities (vHs, Figure 1b).[6−8] Near such vHs, previous studies show that optical absorption increases by ~20% and is peaked at an energy, E_θ.[6,7,9−17] This absorption resonance peak energy increases monotonically with θ (see Supplementary Video 1).[18] To date, however, the properties of electrons photoexcited near these vHs remain unexplored beyond the Raman and linear absorption characterization. Here, we apply space, time, and energy-resolved 1-photon (1-ph) and 2-photon (2-ph) transient absorption (TA) microscopy to both spectrally map the excited state electronic structure of tBLG and spatially resolve the ensuing electronic dynamics.

The single-particle band structure of tBLG can be understood by superimposing two graphene Brillouin zones, rotated by a twist angle θ, as shown in Figure 1a.[19,20] The vertical line cutting through the two Dirac points of the graphene layers (Figure 1b) shows the band anticrossing near the degeneracy with an energy splitting (Δ) and four possible vHs transitions between the graphene sub-bands labeled 1 through 4. These optical transitions experience a large joint density of states between the valence bands (1 and 2) and the conduction bands (3 and 4), but only $1 \rightarrow 3$ (denoted X_{13}) and $2 \rightarrow 4$ (X_{24}) transitions are allowed due to selection rules.[16,21]

Figure 1. (a) tBLG free-electron interlayer band-structure. (b) Cross-sectional view shows interlayer vHs resonances, X_{13} and X_{24}, between band anticrossing regions. (c) Alternatively, the degenerate X_{13} and X_{24} states may rehybridize, giving a 1-ph state above, and a 2-ph allowed exciton state below. TA (arrows) interrogates the electronic population (circles).

Outwardly, the X_{13} and X_{24} transitions shown in Figure 1b are degenerate vHs similar to graphene's M-point saddle-point exciton.[19,22] In this case, Coulombic attraction between $e-h$ pairs would augment both X_{13} and X_{24} transition energies and produce an asymmetric, Fano optical line shape.[23,24] Since such unbound excitons are coupled to continuum states of graphene,[23] this model predicts that the 1-ph TA response from tBLG decays quickly, with an amplitude and rate similar to single-layer graphene (dotted arrow in Figure 1b).

Alternatively, previous studies suggest that inclusion of bound-exciton effects are necessary to simulate the nearly Gaussian tBLG optical absorption line shape.[18,25] While one can consider unbound excitonic states for X_{13} and X_{24} independently, such a picture is incomplete because the two states occur at the same energy and momentum, a direct result of the electron–hole symmetry at the vHs in tBLG. A more complete description was given in recent work reported by Liang et al. that predicts formation of stable, strongly bound ($E_B \sim 0.5$ eV) excitons.[25] These first-principles calculations suggest that interlayer excited states in tBLG are better described by renormalized symmetric ($X_S = X_{13} + X_{24}$) and antisymmetric ($X_A = X_{13} - X_{24}$) excitonic states.[25] In this model, illustrated in Figure 1c, X_S corresponds to the optical tBLG resonance at E_θ and is an unstable exciton state.[7,18] Conversely, X_A is only 2-ph accessible and is calculated to be a strongly bound, localized excitonic state.[25] The remarkable stability predicted for the X_A state results from the deconstructive coherence between the two degenerate Fano resonances serving to cancel the coupling to the continuum interlayer graphene states. Such a state is termed a "ghost Fano" resonance. While similar phenomena have been weakly observed in quantum dot and carbon nanotube systems, such strongly bound exciton states have never been observed in a 2D metallic system.[25−27] If such ghost Fano resonance effects are manifest in tBLG, weak exciton−continuum coupling is expected to stabilize the local exciton population, as observed by a longer electronic recombination time for both the 1-ph (X_S) and 2-ph (X_A) TA response.

In this work, we obtain the TA spectra and dynamics of single tBLG domains and map out the different 1-ph and 2-ph electronic transitions predicted by the contrasting vHs and strongly bound exciton models in Figure 1. We further correlate ultrafast TA microscopy with the precise local atomic stacking and grain boundaries, by employing darkfield TEM to definitively assign a twist angle to the absorption resonance, E_θ.[28] Our experimental TA microscopy approach is outlined in Figure 2a. The 1-ph TA map in Figure 2a shows a prominent patch of 6.8° oriented tBLG that is surrounded by single, and non twisted multilayer graphene on a silicon nitride membrane. This map was obtained by raster scanning a diffraction-limited pump and probe pulse pair over multilayer graphene. We tuned our 140 fs pump pulse to be resonant with the 6.8° domain at $E_{pump} \sim E_\theta \sim 1.3$ eV. After a delay time t, we detect the differential TA ($\Delta R(t) \propto \Delta\sigma(t)$) (see supplementary section 3) of a collinear probe pulse and construct time-dependent TA maps point-wise. Using probe energies ($E_{pr} = 0.8$ eV) well below the resonance E_θ, in Figure 2a graphene gave an interband decreased absorption response (i.e., Pauli blocking of probe beam) everywhere at all time delays.[2]

Our TA maps can be interpreted as "movie frames" that closely approximate the relative photoexcited electronic population at a particular probe energy and time-delay (see Supplementary Video 2). The 6.8° tBLG region labeled in
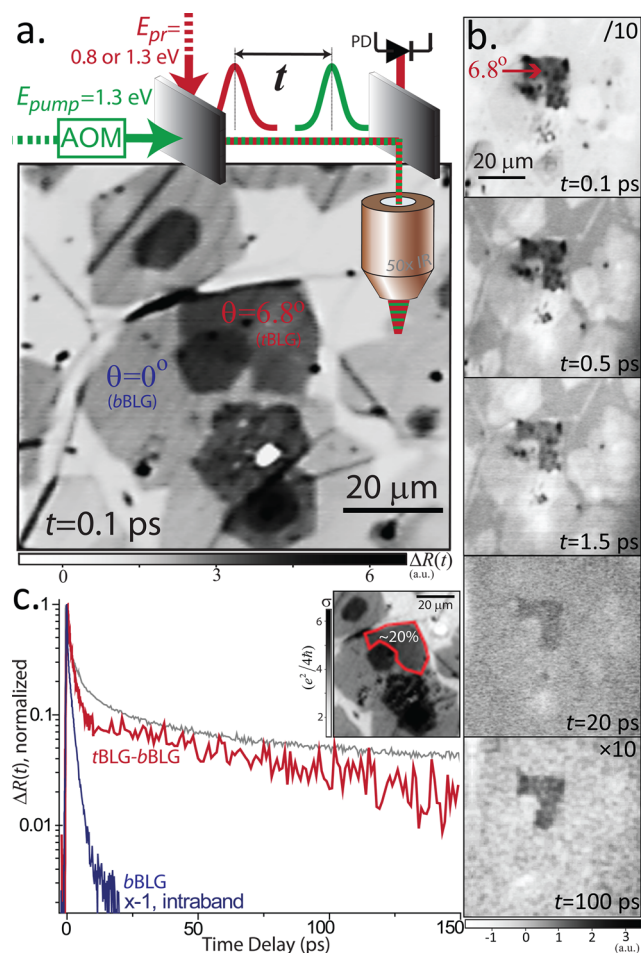
Figure 2. tBLG electronic relaxation bottleneck. (a) Ultrafast scanning TA microscopy map of multilayer graphene. The TA Pauli blocking response is >2× enhanced for the 6.8° tBLG domain. (b) On-resonance TA maps at $E_{pump} \sim E_{pr} = E_\theta$ show a TA response localized to the 6.8° domain is present for t > 100 ps. The surrounding graphene gives only a weak transient intraband response (opposite sign). (c) TA relaxation kinetics of the bBLG and tBLG regions labeled (vs SWNT E_{11} state, gray). Corresponding linear absorption map at 1.3 eV shows tBLG (red) is only ∼20% stronger than in bBLG (inset).

Figure 2a has a ∼ 2-fold stronger TA Pauli blocking response than the adjacent 0° stacked bilayer regions. However, the corresponding linear absorption map in Figure 2c only shows a ∼ 20% resonant enhancement. To account for this discrepancy, electrons in interlayer tBLG avoided crossing regions must relax much slower than the surrounding nontwisted graphene bilayers, suggesting an intrinsic electronic relaxation bottleneck.

In Figure 2b, we repeat the 1-ph measurement but instead *resonantly probe* the electronic population at E_θ ($E_{pump} = 1.33$ eV, $E_{pr} = 1.26$ eV probe). Compared against the corresponding linear absorption map in Figure 2c (inset), the TA maps differ in both sign and absolute amplitude. Strikingly, only the 6.8° tBLG domain gives a strong TA Pauli blocking response. Meanwhile, the surrounding graphene in Figure 2b gives a weak, short-lived graphene intraband TA response signified by its *opposite sign*. This suggests that interlayer tBLG electrons are decoupled from the intraband transient response that dominates the TA map everywhere else in Figure 2b. Surprisingly, the subsequent TA movie frames show that excited carriers are present even >100 ps after initial excitation.
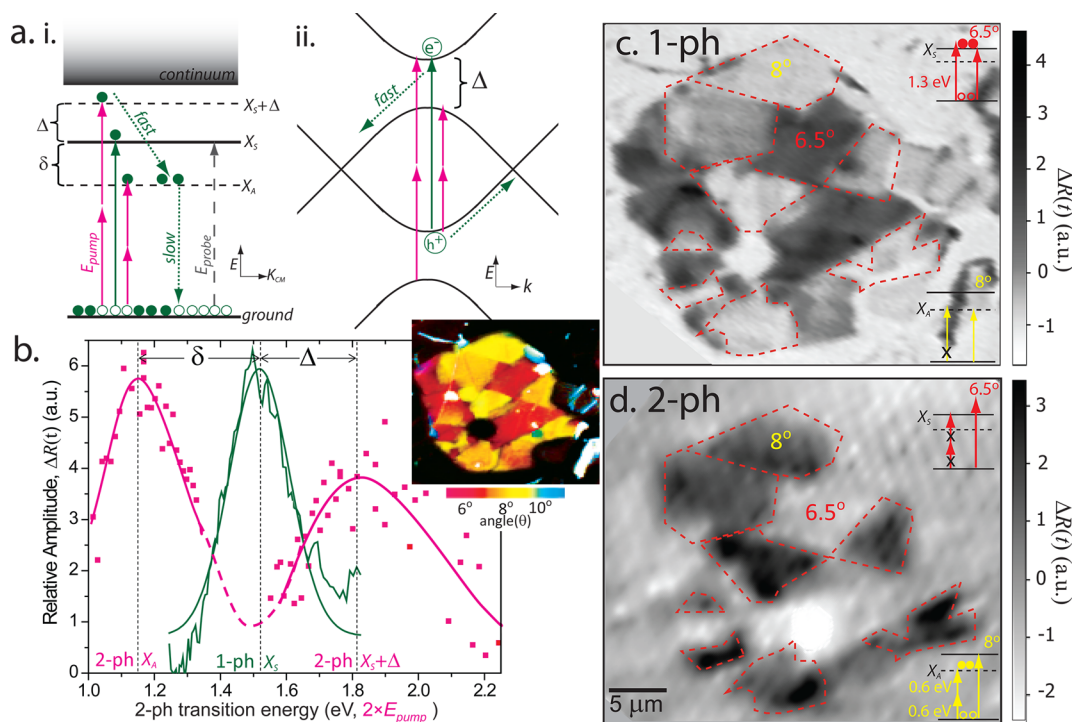
Figure 3. One-photon vs two-photon absorption of ~6.5° and ~8° tBLG domains. (a) Competing models; (i) bound exciton model, (ii) continuum model. (b) 8° tBLG 2-ph transition TA spectrum (magenta), and 1-ph linear absorption spectrum (green, $\sigma_{tBLG} - \sigma_{bBLG}$). The first 2-ph peak fits best to a Gaussian line shape centered at $\delta = 0.37$ eV below E_θ, the second peak has a Fano line shape centered at $\Delta = 0.33$ eV above. (Inset, map of the tBLG absorption resonance vs twist angle.) (c) 1-photon TA map, at $E_{pump} = 1.3$ eV shows a strong electronic bleach only from the resonantly excited 6.5° domains. (d) Conversely, a 2-ph TA map at $E_{pump} = 0.6$ eV shows a ground-state bleach only from the 8° domains (dotted outlines). Combined, these maps demonstrate that the (X_S) state is 1-ph allowed, and the X_A state is only 2-ph allowed.

Both observations definitively show that interlayer electrons excited at E_θ experience a major bottleneck restricting electronic relaxation. Such a strong and long-lived electronic signal in tBLG disagrees with the continuum Fano resonance model (Figure 1b) but can be explained by an excitonic model (Figure 1c) where weak exciton-continuum coupling allows for stable exciton formation.[25]

To isolate the relaxation rates intrinsic to interlayer tBLG electrons excited at E_θ, we plot tBLG-bBLG (red) in Figure 2c by subtracting the much weaker (and opposite signed) intralayer electronic TA response (blue). A similar approach has been previously used to decouple linear absorption spectra, as $\sigma_{tBLG} - \sigma_{bBLG}$.[13,16] A least-squares deconvolution exponential fit of the kinetic decay requires only a biexponential fit that decays with lifetimes of 1.4 ± 0.1 ps and 66 ± 4 ps. These lifetime components are remarkably long for any electronic state within a metallic system. By repeating our linear and TA measurements at low temperatures, we further found that the interlayer electronic response appears largely invariant to both lattice temperature (5−295 K) and the substrate used (see Supporting Information). Furthermore, the TA response does not shift sign as the probe wavelength was scanned through the resonance, E_θ. Combined, these observations suggest that laser-induced heating effects do not contribute appreciably to the overall large TA signal response, and so the TA signal is predominately electronic in origin.

If electronic carriers in tBLG are unbound excitons, the TA (red) in Figure 2c must relax at a rate similar to bBLG (navy), providing that phonons with $E > \Delta$ (dotted arrow in Figure 1b) are available to scatter carriers through the anticrossing gap (Δ) illustrated in Figure 1b.[2] Comparison of the short-time tBLG

kinetics against bBLG in Figure 2c (red) reveals the absence of the dominant fast subps electron relaxation components associated with graphene electron thermalization and optic phonon emission.[14] Remarkably, the shortest interlayer tBLG lifetime is 1.4 ps, which is similar to graphene's rate-limiting relaxation rate that is often associated with disorder-assisted or supercollision relaxation.[2,29] The absence of the subpicosecond relaxation processes, and the emergence of this long ~66 ps decay in tBLG relaxation kinetics, suggests that \ electrons are initially decoupled from graphene's continuum states, as predicted by the strongly bound exciton model.[25]

The unexpected TA relaxation bottleneck we observe in Figure 2c is further compared against semiconducting single-walled carbon nanotubes (SWCNTs), another carbon-based system with constrained 2p orbital interactions. It is established that SWCNTs have 1-ph and 2-ph allowed excitonic states that form by (chiral) angle dependent overlap of 2p orbitals.[30−32] Figure 2c (gray) plots the E_{11} exciton relaxation rate of (6,5) chirality SWCNTs against tBLG (red). While the short time behavior differs greatly, Figure 2c shows the longer components of both traces decay at a similar rate, suggesting that the dynamic phonon environment causing E_{11} exciton relaxation in SWCNTs might be of a similar nature to the interlayer exciton−phonon interactions causing exciton relaxation in tBLG.

We can better distinguish between competing vHs and bound exciton models outlined in Figure 3a, by exploiting the 2-ph selection rules required for the predicted dark tBLG exciton state, X_A.[21,25] To search for possible dark state transitions, we used a different sample of CVD bilayer graphene. The linear absorption map shown in Figure 3b

(inset) reveals a series of *t*BLG domains with twist angles of either ~6.5° (red) or ~8° (yellow), corresponding to $E_\theta \sim 1.25$ and 1.52 eV respectively. Figure 3b plots the 2-ph TA spectrum obtained using IR pump energies ranging from $E_{pump} = 0.49$ to 1.15 eV, and a 8° resonant probe at $E_\theta \sim E_{pr} = 0.56$ eV. We observe two clear TA peaks centered at 1.18 and 1.82 eV that originate from a resonantly enhanced 2-ph absorption. Specifically, as illustrated in Figure 3ai, we observe these dark states through resonant 2-ph enhanced Pauli blocking of the depleted ground state. Moreover, our ability to probe electronic population of optically dark state requires that X_S and X_A states share a common ground state; an inherent feature of a bound exciton model.[32]

The lowest peak in Figure 3b indicates that enhanced 2-ph absorption took place via a discrete, low-lying transition centered at 1.18 eV. Comparing the 2-ph peak against the 1-ph absorption resonance at $E_\theta = 1.52$ eV (green, Figure 3b), we readily obtain the energy-state splitting parameters of $\delta = 0.37$ eV and $\Delta = 0.33$ eV. This 0.37 eV energy splitting closely matches the theoretically predicted $\delta \cong 0.4{-}0.5$ eV, state splitting calculated for 21° *t*BLG.[25] Such a large bright-dark state energy splitting is much greater than the analogous state splitting in SWCNTs and explains why photoluminescence has not yet been observed from resonantly excited *t*BLG domains.

To completely map the selection rules associated with *t*BLG electronic transitions, we compare the 1- and 2-ph TA microscopy response of 6.5° and 8° oriented domains in Figure 3c–d. Figure 3c maps-out the 1-ph TA response for $E_{pump} = 1.3$ eV and $E_{pr} = 1.2$ eV at $t = 0.3$ ps. Despite the X_A state being 1-ph resonant with the ~8° *t*BLG (dotted red outlines), we observed only a weak intraband response as was seen for *b*BLG regions previously (Figure 2b). This confirms that the X_A transition is not 1-ph accessible. In contrast, the 6.5° *t*BLG domains give a strong Pauli blocking response because E_{pump} is resonant with X_S.

2-ph resonant transitions of single *t*BLG domains are imaged in Figure 3c, by tuning our pump pulse energy to roughly half the predicted 8° X_A state energy (see Figure 3a) or $E_{pump} = 0.6$ eV. Comparison of the TA maps in Figure 3c against d show all of the 8° *t*BLG domain excitations that were forbidden under 1-ph excitation conditions are now allowed for a 2-ph excitation. Conversely, all of the 6.5° *t*BLG domain excitations that were observed under 1-ph excitation conditions now appear dark (inaccessible) under two-photon excitation. Using state parity, we assign the two-photon accessible dark states in Figure 3d to electronic carriers populating the X_A state of 8° *t*BLG. Together, Figure 3c and d shows that the X_S bright state is two-photon forbidden, and the dark X_A state is only two-photon allowed. These strongly enforced selection rules follow the parity expectations of a roughly hydrogenic-like, strongly bound exciton model advocated by recent first-principle simulations.[25]

The 2-ph spectral peak centered at 1.82 eV in Figure 3b has not been previously predicted or observed. This peak has a broader, asymmetric shape, which fits better to a Fano line shape expected from the unbound exciton model.[33,34] In contrast, the other 1-ph and 2-ph peaks in Figure 3b fit best to a Gaussian line shape, a common characteristic of bound excitonic transitions. Accordingly, we infer that the two-photon absorption near 1.82 eV is best assigned to an unbound state transition labeled $X_S + \Delta$ in Figure 3a,i. Conversely, the two-photon absorption resonance lying $\delta = 0.37$ eV below is best characterized as the X_A bound exciton or ghost Fano resonance

peak predicted by Liang et al.[25] as supported by (i) its asymmetric energy spacing (i.e., δ vs Δ), (ii) Gaussian line shape, (iii) long electronic lifetime, and (iv) parity enforced two-photon selection rules for the X_A and X_S transitions.

Using both explicit calculations based on the Bethe–Salpeter equation and effective low-angle continuum model, Liang et al. predicted radically different electronics properties emerging for both the theorized X_S and X_A exciton states.[25] Specifically, the symmetric X_S state was found to have delocalized wave functions and a negligible binding energy. Conversely, the antisymmetric state X_A is predicted to be optically dark, insensitive to $e{-}h$ charge screening, and strongly bound.[25] While certain phonons can scatter bound excitons into the lower-lying continuum states, the exciton-continuum coupling for the X_A is predicted to be vanishingly small and roughly intensive to charge screening effects.[25] Accordingly, both theory and our TA microscopy now support that fast exciton dissociation becomes unfavorable in the X_A state of *t*BLG, enabling stable and metastable bound exciton states to form.

In Figure 4, we compare the 1-ph X_S (pink) vs 2-ph X_A (black) electron relaxation kinetics measured on 8° oriented
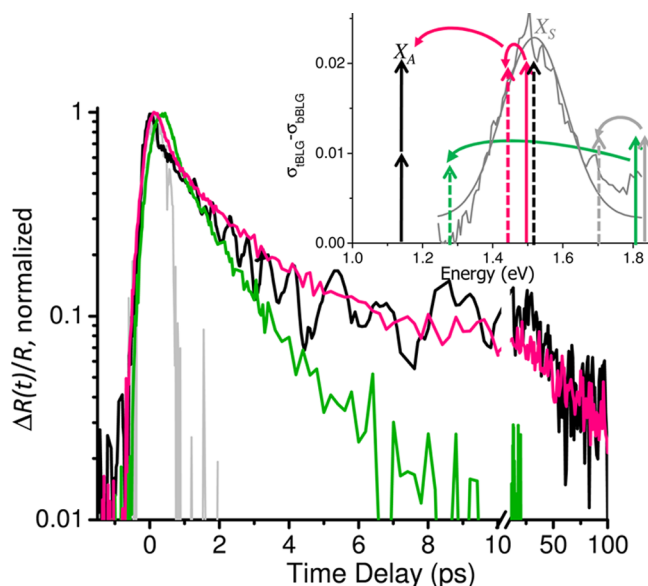
Figure 4. Resonant vs nonresonant electronic relaxation for 8° *t*BLG. The vertical pump (solid arrows) and probe (dashed arrows) combinations labeled on the absorption spectrum (inset) of 8° *t*BLG, correspond by color to the normalized 1- or 2-ph. relaxation kinetics plotted.

*t*BLG. We find that the normalized TA relaxation kinetics for one-photon and two-photon resonant excitations are nearly identical. Such similar kinetic decay suggests that both signals originate from the same depleted common ground state, and that the electrons impulsively relax from the bright (X_S) to the dark (X_A) state as illustrated in Figure 3a,i. Such fast kinetic $X_S \rightarrow X_A$ relaxation is consistent with theory showing that X_S is an unstable exciton state.[25] As a control, in Figure 4 (gray) we show that the relaxation kinetics are impulsive when both E_{pump} and $E_{pr} > E_\theta$, indicating that only free electron states are probed above resonance. Lastly, we consider the case of $E_{pr} < E_\theta < E_{pump}$ (green trace). We show the long-decay components are consistently absent, suggesting resonant optical excitation may be required to form a long-lived stable exciton state. Nonetheless, the off-resonance *t*BLG kinetic relaxation

(green) is still significantly enhanced in amplitude and lifetime compared to the *b*BLG TA response (Figure 2c). This suggests that an electronic relaxation bottleneck effect is still present even when *t*BLG is optically excited above resonance.

By definitively isolating the interlayer electronic dynamics of 1- and 2-ph resonant optical transitions in *t*BLG, we have uncovered a fine-structure of bound (X_A) and unbound (X_S) exciton states that agrees well with recent simulations.[25] Specifically, we employed a novel form of diffraction-limited TA microscopy to obtain the intrinsic spectra and dynamics of single *t*BLG domains under a variety of resonant and nonresonant pump/probe combinations. In Figure 2b, we show a TA movie of electronic population that reveals the striking contrast between the bound-exciton carrier population inside the *t*BLG domain and the free-electron population in the surrounding graphene. These results suggest that the photo-excited *t*BLG interlayer electrons are initially decoupled from scattering into graphene continuum states, experiencing a significant electron relaxation bottleneck. In particular, resonantly excited carriers in *t*BLG give a many-fold enhanced TA amplitude, with longer relaxation kinetics for both the short (∼2 ps) and long relaxation time scales (∼70 ps). This bottleneck is best explained by the existence of strongly bound excitons in a "ghost Fano" state that we explicitly resolve using 2-ph TA microscopy.[25] Our results imply that *t*BLG may be a unique hybrid electronic material where free-electron metallic character can coexists alongside stable exciton states. The work further opens up possible new avenues for carrier extraction that combine the high conductivity of metallic *intra*layer-electrons, with the enhanced electronic population that is now established for the *inter*layer electrons in *t*BLG.

Methods. Multilayer graphene was grown using low pressure CVD method on copper foil and transferred to silicon nitride grids (see Supporting Information).[35] Areas containing low-angle *t*BLG were first identified using a combination of hyperspectral absorption imaging technique and dark field TEM (DF-TEM). Final twist angle assignments of the bilayer patches were made by correlating the linear absorption and 1-ph TA spectral peak energies.[13,18]

*t*BLG bright (X_S) and dark (X_A) states and their corresponding electronic dynamics were measured using 1- and 2-ph confocal scanning TA microscopy.[36] Collinear pump-and probe pulses were obtained from two independently tunable outputs of an ultrafast system composed of Ti:Saph oscillator (Coherent Chameleon Ultra II, 80 MHz, wavelength range 680−1080 nm) pumping an optical parametric oscillator (APE-Compact, wavelength range 1000−4000 nm). For one-photon TA measurements requiring pump and probe pulse doubly resonant with the bright (X_S) transition, a white-light supercontinuum probe was instead used. Cross-correlation of the pump and probe after the objective yielded a fwhm pulse duration of 142 fs.

After a mechanical delay stage, both the pump and the probe beams were aligned in a collinear geometry, raster-scanned by piezo-scanning mirror and coupled into a confocal scanning microscope via a 50X IR-region enhanced, achromatic objective (NA = 0.65). One- and two-photon transient absorption signals were detected by measuring the probe beam on with a TE cooled InGaAs detector connected to a Zurich HF2LI lock-in amplifier. The pump beam was modulated at either 0.25 or 1 MHz using a AO-modulator (Gooch & Housego) to enable high-frequency lock-in detection of the differential reflectivity. Appropriate optical filters were used in front of the detector to block the pump beam. The pump and probe spot sizes on the sample were determined to ∼1.5 *μ*m, by fitting to a confocal scanning reflection profile of deposited gold pads. The fluence of the probe power was 5% of the pump fluence. Except where specified, all of the measurements were done at 295 K. The probe power was fixed at $(∼1 × 10^{12}$ photons/cm$^2)$ for the pump power dependence measurements. Microscope objective/transmission correction curves were measured and rigorously taken into account for all the wavelengths, after each measurement.

■ ASSOCIATED CONTENT

Ⓢ Supporting Information

The Supporting Information is available free of charge on the ACS Publications website at DOI: 10.1021/acs.nano-lett.5b02035.

> Details of fabrication and characterization of *t*BLG, experimental set up, optical conductivity of *t*BLG, lattice temperature and substrate dependence, one and two photon flux dependence (PDF)
> Hyperspectral absorption microscopy of *t*BLG (AVI)
> Ultrafast transient absorption microscopy of graphene (AVI)
> Ultrafast transient absorption microscopy of *t*BLG (AVI)

■ AUTHOR INFORMATION

Corresponding Author
*E-mail: graham@physics.oregonstate.edu.

Notes

The authors declare no competing financial interest.

■ ACKNOWLEDGMENTS

■ REFERENCES

(1) Malard, L. M.; Fai Mak, K.; Castro Neto, A. H.; Peres, N. M. R.; Heinz, T. F. *New J. Phys.* **2013**, *15*, 015009.

(2) Graham, M. W.; Shi, S.-F.; Wang, Z.; Ralph, D. C.; Park, J.; McEuen, P. L. *Nano Lett.* **2013**, *13*, 5497−5502.

(3) Ju, L.; Shi, Z.; Nair, N.; Lv, Y.; Jin, C.; Velasco, J., Jr; Ojeda-Aristizabal, C.; Bechtel, H. A.; Martin, M. C.; Zettl, A.; Analytis, J.; Wang, F. *Nature* **2015**, *520*, 650−655.

(4) Tielrooij, K. J.; Piatkowski, L.; Massicotte, M.; Woessner, A.; Ma, Q.; Lee, Y.; Myhro, K. S.; Lau, C. N.; Jarillo-Herrero, P.; van Hulst, N. F.; Koppens, F. H. L. *Nat. Nanotechnol.* **2015**, *10*, 437−443.

(5) Newson, R. W.; Dean, J.; Schmidt, B.; van Driel, H. M. *Opt. Express* **2009**, *17*, 2326.

(6) Li, G.; Luican, A.; Lopes dos Santos, J. M. B.; Castro Neto, A. H.; Reina, A.; Kong, J.; Andrei, E. Y. *Nat. Phys.* **2009**, *6*, 109−113.

(7) Lui, C. H.; Li, Z.; Chen, Z.; Klimov, P. V.; Brus, L. E.; Heinz, T. F. *Nano Lett.* **2010**, *11*, 164−169.

(8) Park, J.; Mitchel, W. C.; Elhamri, S.; Grazulis, L.; Hoelscher, J.; Mahalingam, K.; Hwang, C.; Mo, S.-K.; Lee, J. *Nat. Commun.* **2015**, *6*, 5677.

(9) Jorio, A.; Kasperczyk, M.; Clark, N.; Neu, E.; Maletinsky, P.; Vijayaraghavan, A.; Novotny, L. *Nano Lett.* **2014**, *14*, 5687−5692.

(10) Bistritzer, R.; MacDonald, A. H. *Proc. Natl. Acad. Sci. U. S. A.* **2011**, *108*, 12233−7.

(11) Luican, A.; Li, G.; Reina, A.; Kong, J.; Nair, R. R.; Novoselov, K. S.; Geim, A. K.; Andrei, E. Y. *Phys. Rev. Lett.* **2011**, *106*, 126802.

(12) Grüneis, A.; Attaccalite, C.; Wirtz, L.; Shiozawa, H.; Saito, R.; Pichler, T.; Rubio, A. *Phys. Rev. B: Condens. Matter Mater. Phys.* **2008**, *78*, 205425.

(13) Havener, R. W.; Zhuang, H.; Brown, L.; Hennig, R. G.; Park, J. *Nano Lett.* **2012**, *12*, 3162−3167.

(14) Wang, Y.; Ni, Z.; Liu, L.; Liu, Y.; Cong, C.; Yu, T.; Wang, X.; Shen, D.; Shen, Z. *ACS Nano* **2010**, *4*, 4074−80.

(15) Brihuega, I.; Mallet, P.; González-Herrero, H.; Trambly de Laissardière, G.; Ugeda, M. M.; Magaud, L.; Gómez-Rodríguez, J. M.; Ynduráin, F.; Veuillen, J.-Y *Phys. Rev. Lett.* **2012**, *109*, 196802.

(16) Havener, R. W.; Liang, Y.; Brown, L.; Yang, L.; Park, J. *Nano Lett.* **2014**, *14*, 3353−3357.

(17) Carozo, V.; Almeida, C. M.; Fragneaud, B.; Bedê, P. M.; Moutinho, M. V. O.; Ribeiro-Soares, J.; Andrade, N. F.; Souza Filho, A. G.; Matos, M. J. S.; Wang, B.; Terrones, M.; Capaz, R. B.; Jorio, A.; Achete, C. A.; Cancado, L. G. *Phys. Rev. B: Condens. Matter Mater. Phys.* **2013**, *88*, 085401.

(18) Havener, R. W.; Kim, C.-J.; Brown, L.; Kevek, J. W.; Sleppy, J. D.; McEuen, P. L.; Park, J. *Nano Lett.* **2013**, *13*, 3942−3946.

(19) Mele, E. J. *Phys. Rev. B: Condens. Matter Mater. Phys.* **2010**, *81*, 161405.

(20) Lopes dos Santos, J. M. B.; Peres, N. M. R.; Castro Neto, A. H. *Phys. Rev. Lett.* **2007**, *99*, 256802.

(21) Moon, P.; Koshino, M. *Phys. Rev. B: Condens. Matter Mater. Phys.* **2013**, *87*, 205404.

(22) Mak, K. F.; Shan, J.; Heinz, T. F. *Phys. Rev. Lett.* **2011**, *106*, 046401.

(23) Ohta, T.; Robinson, J. T.; Feibelman, P. J.; Bostwick, A.; Rotenberg, E.; Beechem, T. E. *Phys. Rev. Lett.* **2012**, *109*, 186807.

(24) Fano, U. *Phys. Rev.* **1961**, *124*, 1866−1878.

(25) Liang, Y.; Soklaski, R.; Huang, S.; Graham, M. W.; Havener, R.; Park, J.; Yang, L. *Phys. Rev. B: Condens. Matter Mater. Phys.* **2014**, *90*, 115418.

(26) Lu, H.; Lü, R.; Zhu, B.-f. *Phys. Rev. B: Condens. Matter Mater. Phys.* **2005**, *71*, 235320.

(27) Guevara, M.; Claro, F.; Orellana, P. *Phys. Rev. B: Condens. Matter Mater. Phys.* **2003**, *67*, 195335.

(28) Brown, L.; Hovden, R.; Huang, P.; Wojcik, M.; Muller, D. A.; Park, J. *Nano Lett.* **2012**, *12*, 1609−1615.

(29) Graham, M. W.; Shi, S.-F.; Ralph, D. C.; Park, J.; McEuen, P. L. *Nat. Phys.* **2013**, *9*, 103−108.

(30) Srivastava, A.; Htoon, H.; Klimov, V.; Kono, J. *Phys. Rev. Lett.* **2008**, *101*, 087402.

(31) Matsunaga, R.; Matsuda, K.; Kanemitsu, Y. *Phys. Rev. Lett.* **2008**, *101*, 147404.

(32) Deslippe, J.; Spataru, C. D.; Prendergast, D.; Louie, S. G. *Nano Lett.* **2007**, *7*, 1626−30.

(33) Mak, K. F.; Shan, J.; Heinz, T. F. *Phys. Rev. Lett.* **2011**, *106*, 046401.

(34) Chae, D.-H.; Utikal, T.; Weisenburger, S.; Giessen, H.; Klitzing, K. V.; Lippitz, M.; Smet, J. *Nano Lett.* **2011**, *11*, 1379−82.

(35) Li, X.; Magnuson, C. W.; Venugopal, A.; Tromp, R. M.; Hannon, J. B.; Vogel, E. M.; Colombo, L.; Ruoff, R. S. *J. Am. Chem. Soc.* **2011**, *133*, 2816−2819.

(36) Hartland, G. V. *Chemical Science* **2010**, *1*, 303−309.